Figure S1. MESF Calibration and linear regression of Alexa fluor 488 (AF488) and 647 (AF647) fluorescence channels, A) AF488 fluorescence histogram of a mixture of Quantum™ MESF Alexa Fluor 488 beads detected by side light scattering. Calibration curve relating the MESF values of beads to their measured mean fluorescent intensity taken from the histogram. B) AF647 fluorescence histogram of a mixture of Quantum™ MESF Alexa Fluor 647 beads detected by side light scattering. Calibration curve relating the MESF values of beads to their measured mean fluorescent intensity taken from the histogram.
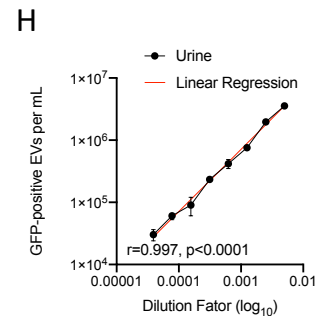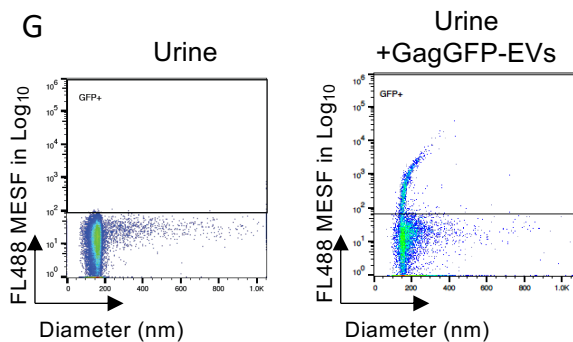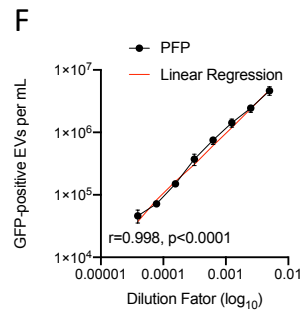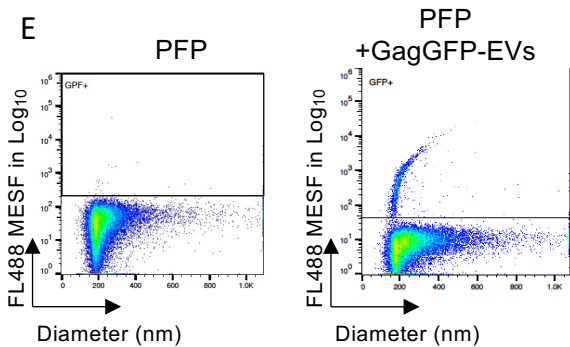
A
HEK293T Wild-Type
HEK293T GFP
HEK293T CD63GFP
HEK293T gagGFP

B
C

D
HEK293T Wild-Type EVs (RI<1.45)
HEK293T gagGFP-EVs (RI≤1.45)

E
PFP
PFP +GagGFP-EVs

F
PFP
Linear Regression
r=0.998, p<0.0001

G
Urine
Urine +GagGFP-EVs

H
Urine
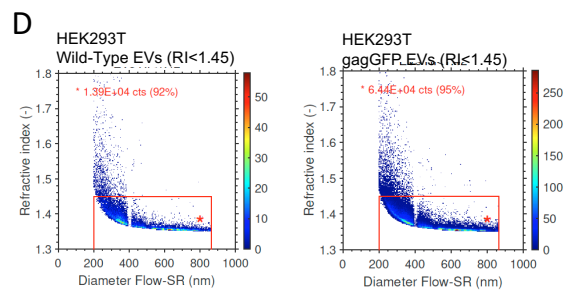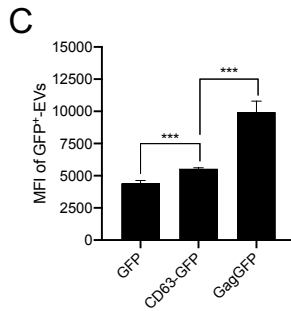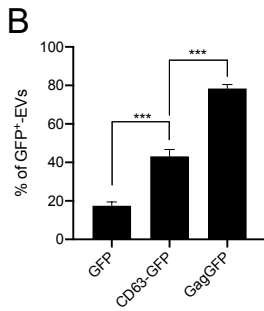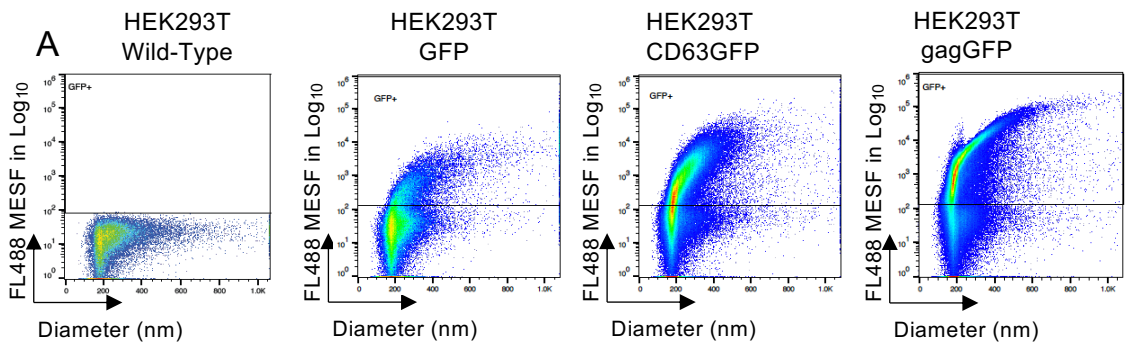Linear Regression
r=0.997, p<0.0001

Figure S2. Sensitive detection of fluorescent recombinant EVs spiked-in biofluids by nanoscale flow cytometry. A) Representative cytograms exhibiting the populations of EVs detected from conditioned cell culture medium of HEK293T wild type cells and HEK293T cells expressing recombinant GFP, CD63-GFP and gag-GFP. X axis represents side scattering based size detection in nanometers and Y axis represents fluorescence intensity of GFP in molecules of equivalent soluble fluorochrome (MESF). B) Percentages of each recombinant GFP-positive EV concentration compared to total particle concentration. C) Mean fluorescence intensity measurement of each recombinant GFP, CD63-GFP and Gag-GFP-positive EV group. D, F) Representative cytograms displaying the detection of GagGFP EVs from patient platelet-free plasma (N=3) and urine (N=3) samples with and without Gag-GFP-positive EV spike-in. X axis represents side scattering based size detection and Y axis represents fluorescence intensity of GFP. E, G) Concentrations of GagGFP-EVs measured in serial dilution of platelet-free plasma and urine samples (N=3/each). Dilution factors are presented in logarithmic scale. Perfect linear regression curve is presented in red (r^2=1).
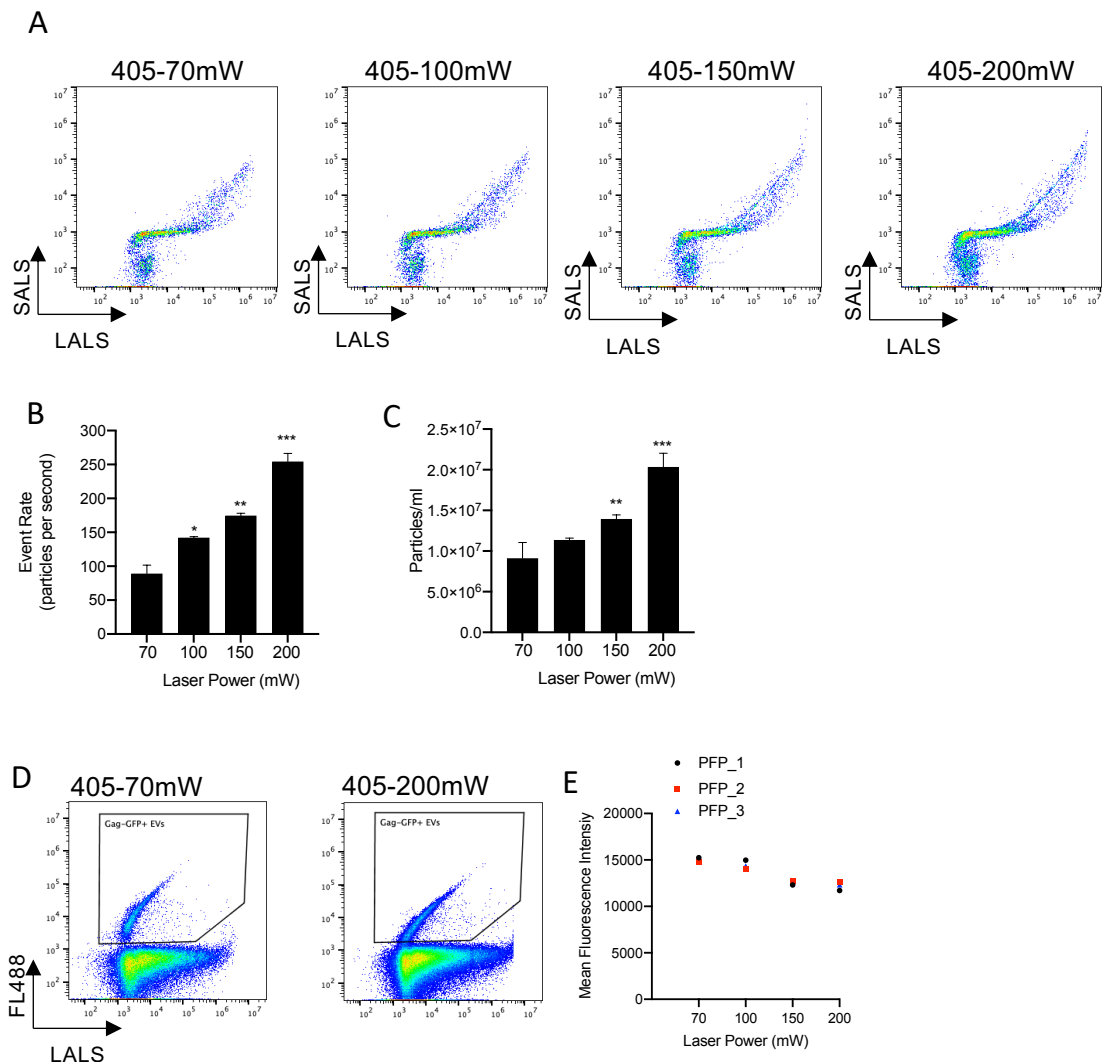
Figure S3. Impact of laser power on side scatter and fluorescence detection of particles. A) Representative nanoscale flow cytometry cytograms showing the detection of total particles in PBS measured in different laser powers. X axis represents side scattering based size detection and Y axis represents forward scattering based size detection. Laser powers are presented in mW. B) The rates of total particle detection from PBS measured in different laser powers. Laser powers are presented in mW. C) The comparison of total particle concentrations in PBS measured in each laser power. D) Representative scatterplots and graph showing the decrease in fluorescence intensity of Gag-GFP+ EVs spiked-in plasma at 70mW and 200mW of 405-nm excitation laser. E) Comparison of mean fluorescence intensities of Gag-GFP+ EVs spiked plasma samples for each laser power.
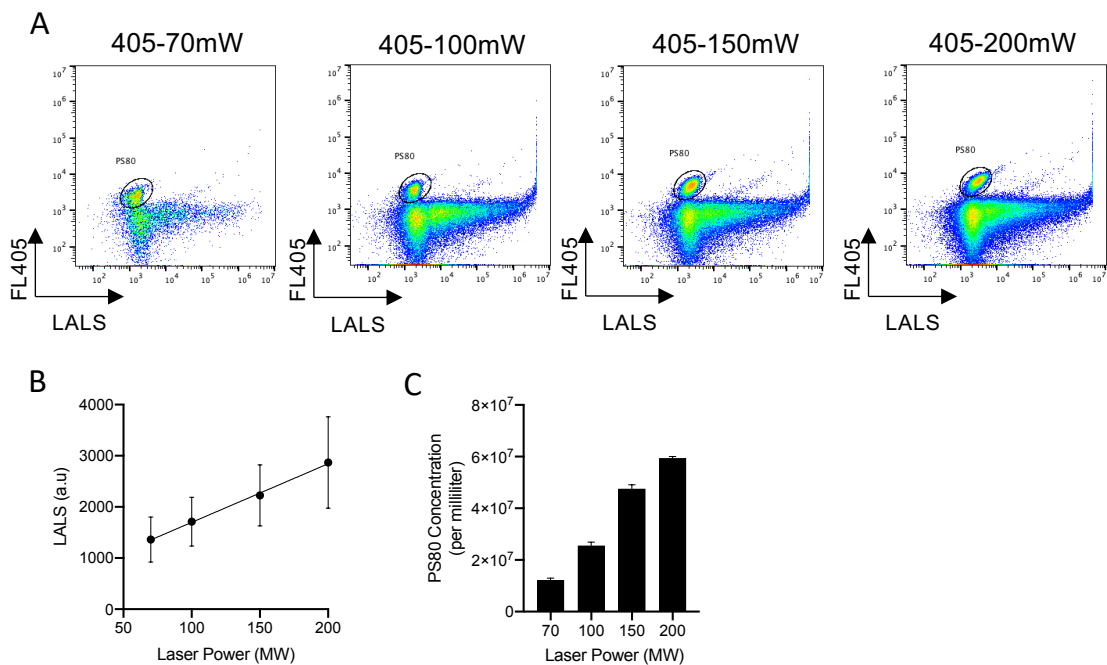
Figure S4. Impact of laser power on side scatter detection of NIST 80nm calibration beads. A) Representative nanoscale flow cytometry cytograms showing the detection of NIST traceable 80 nm polystyrene beads measuring side scatter intensities detected in different laser powers. X axis represents side scattering based size detection and Y axis represents fluorescence intensity of beads. B) Changes in side scatter intensities of beads measured in different laser powers. Side scatter intensities are presented in arbitrary unites and laser powers are presented in mW. C) Concentrations of 80 nm polystyrene beads measured in each laser power.
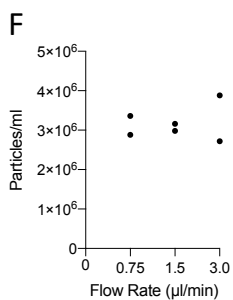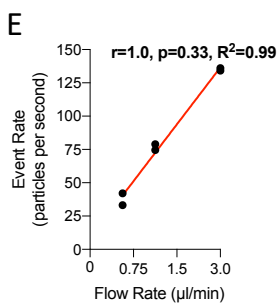
A

LALS 2300   LALS 2000   LALS 1800

B

Event Rate (particles per second)

3000
2500
2000
1500
1000
500
0

***   ***

23   20   18

LALS Threshold (x100 a.u)

C

Particles/ml

2.5×10⁸
2.0×10⁸
1.5×10⁸
1.0×10⁸
5.0×10⁷
0.0

***   ***

23   20   18

LALS Threshold (x100 a.u)

D

FR 0.75 µl/min   FR 1.5 µl/min   FR 3.0 µl/min

E

r=1.0, p=0.33, R²=0.99

Event Rate (particles per second)

150
125
100
75
50
25
0

0   0.75   1.5   3.0

Flow Rate (µl/min)

F

Particles/ml

5×10⁶
4×10⁶
3×10⁶
2×10⁶
1×10⁶
0

0   0.75   1.5   3.0
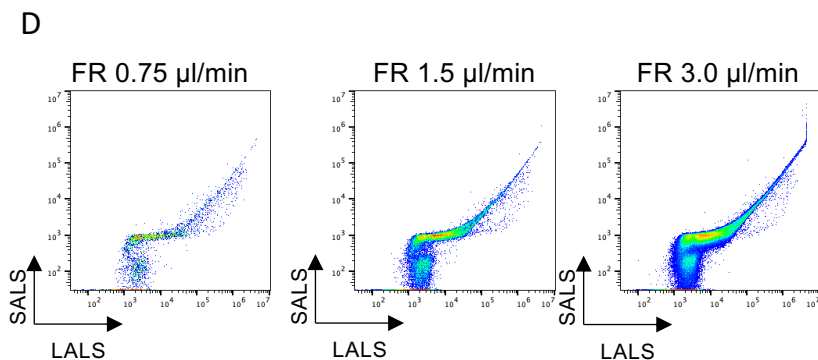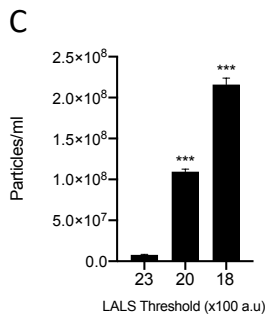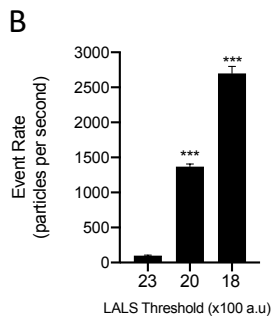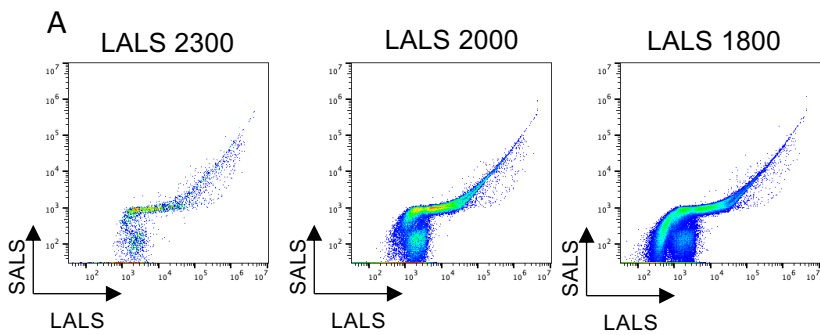
Flow Rate (µl/min)

Figure S5. Impact of side scatter triggering threshold on detection of particles in PBS. A) Representative nanoscale flow cytometry cytograms showing the detection of total particles in PBS measured in different triggering thresholds (a.u). X axis represents side scattering based size detection and Y axis represents forward scattering based size detection. B) The rates of total particle detection per each second from PBS measured in triggering thresholds (a.u). C) The concentration measurement of total particle in PBS measured in each triggering thresholds. D) Representative nanoscale flow cytometry cytograms showing the detection of total particles in PBS measured in different flow rates. X axis represents side scattering based size detection and Y axis represents forward scattering based size detection. E) The rates of total particle detection per each second from PBS measured in different flow rates (μl/min). F) The concentration measurement of total particles in PBS measured in each flow rate.
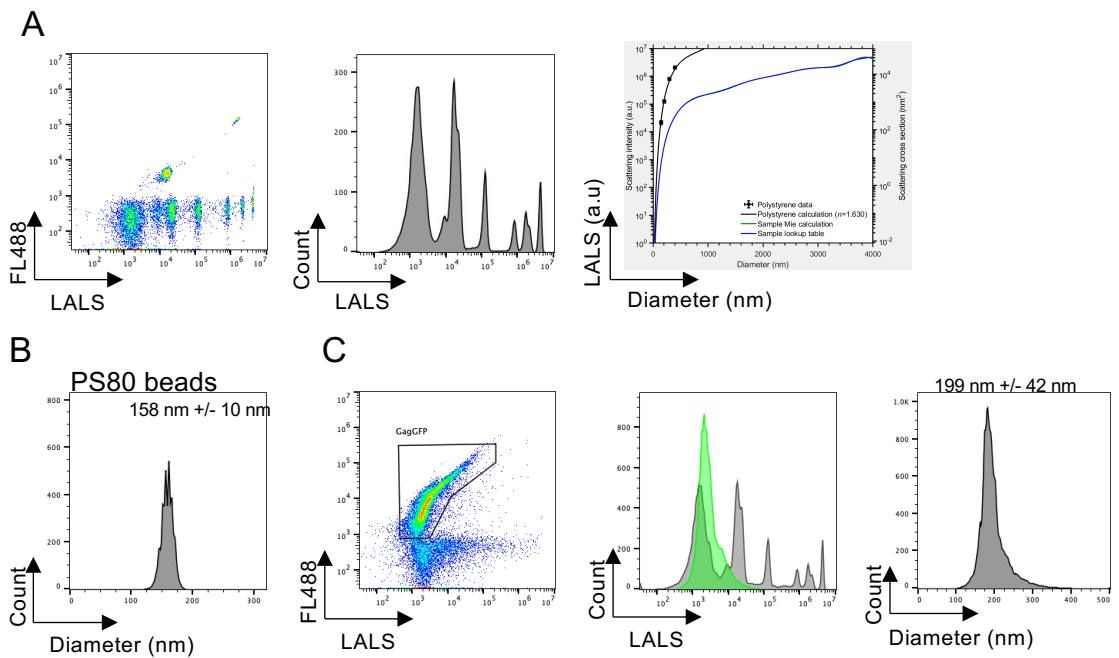
Figure S6. Calibration of side scatter detection of particles by nanoscale flow cytometry. A) Representative cytogram and histogram of a mixture of fluorescent and non-fluorescent polystyrene beads analyzed by nanoscale flow cytometry. Mie theory modeling applied to transform light-scatter intensities into diameters in nanometers based on refractive index of beads and nanoscale flow cytometry. B) Representative histogram of 80nm polystyrene beads with mean diameters and standard deviation in nanometers. C) Representative cytogram and histograms of rEVs from conditioned cell medium of GagGFP expressing HEK293T analyzed by nanoscale flow cytometry. Conversion of mean diameter and standard deviation of GFP-positive EVs was estimated using the scatter-to-diameter relationship.
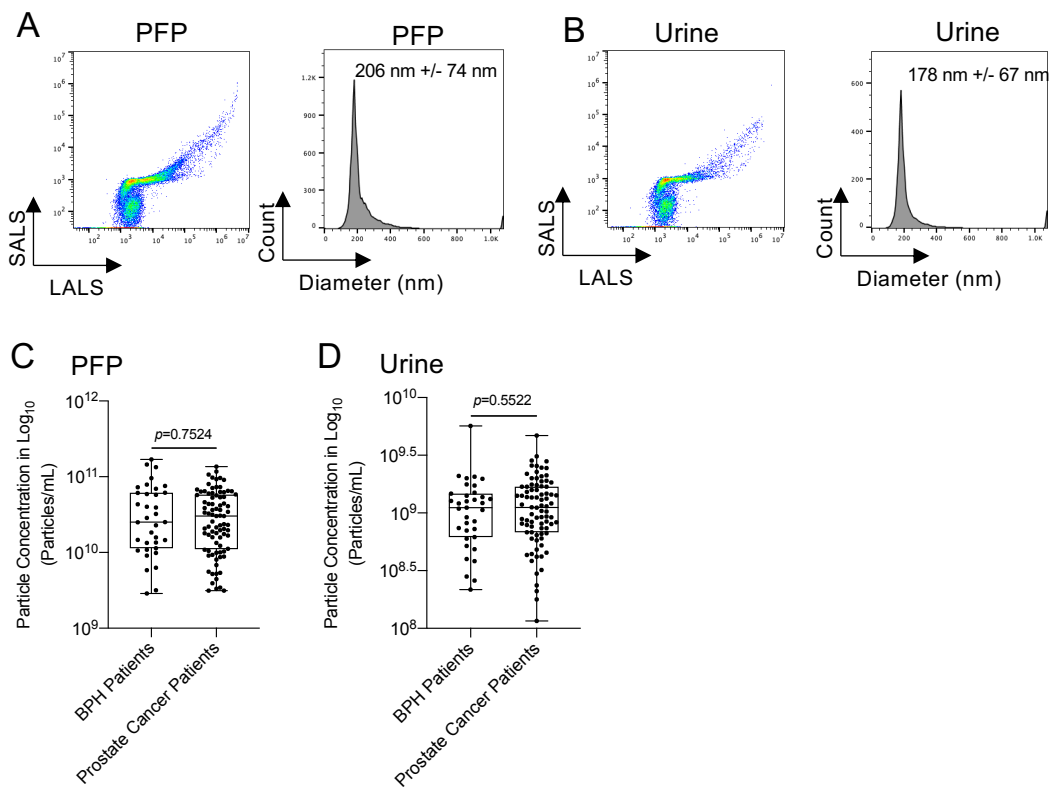
Figure S7. Label-free detection and enumeration of particles from biofluids of localized prostate cancer patients and age-matched BPH patients without standardization. (A, B) Representative cytograms showing total particle detection from plasma and urine samples of localized prostate cancer patients (N=85) and BPH (N=35) patients, and corresponding histograms exhibiting median diameters and standard deviation in nanometers of plasma and urinary particles respectively. C, D) Concentrations of particles detected in PFP and urine particles from BPH (N=35) and prostate cancer patients (N=85) respectively.
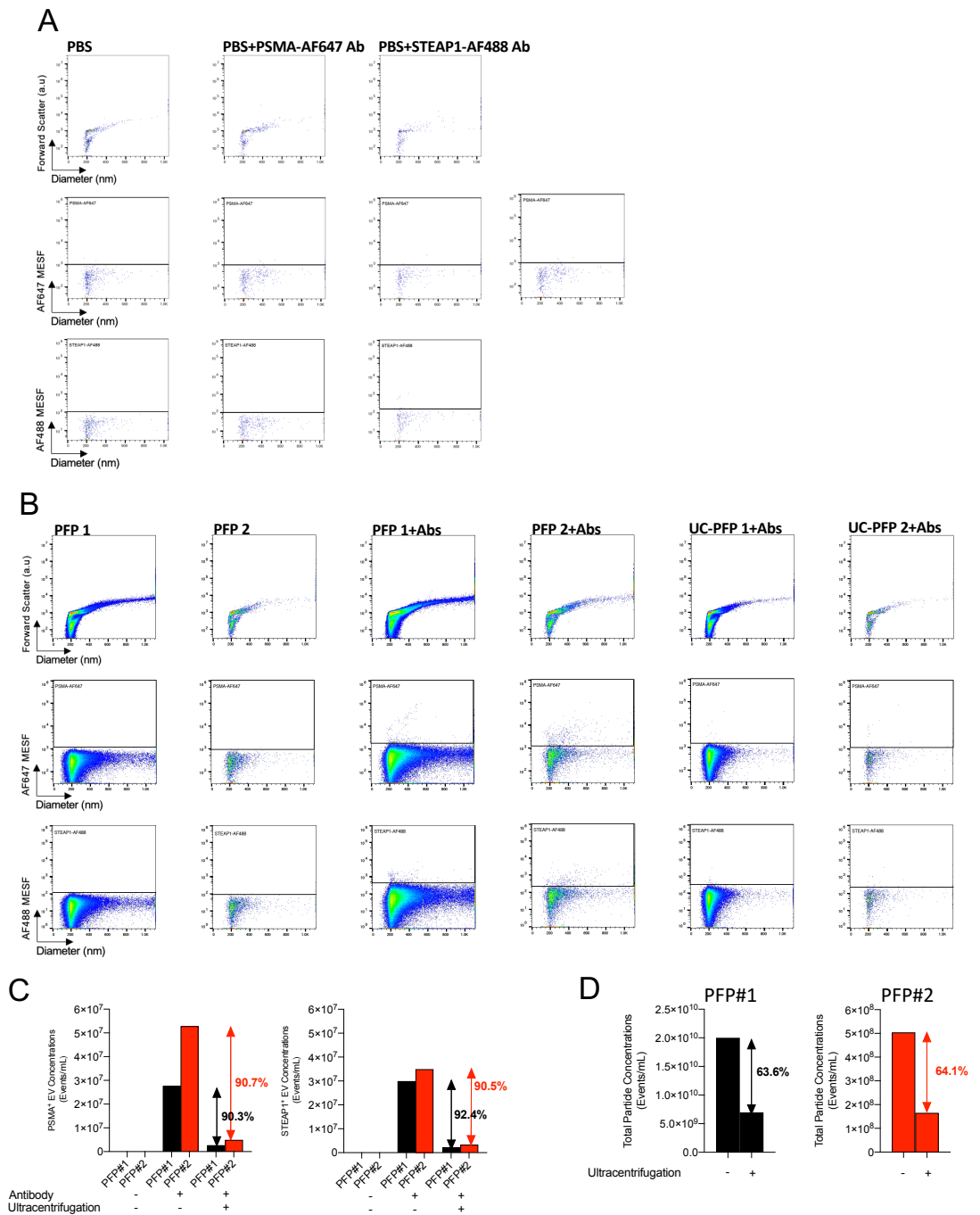
Figure S8. Evaluation of antibody specificity for detection of prostate-derived EVs using ultracentrifugation-based EV depletion in human plasma. (A) Representative cytograms of buffer only and buffer with antibodies. X-axis represents diameter (nm), Y-axis represents forward light scatter (a.u), and MESF of AF647 and AF488 respectively. (B) Representative cytograms of without and with PSMA-AF647 and STEAP1-AF488 antibodies, and cytograms of PFP#1 and PFP#2 with PSMA-AF647 and STEAP1-AF488 antibodies after ultracentrifugation of plasma samples. (C, D) Comparison of concentrations of total particles, PSMA+ EVs, and STEAP1+ EVs before and after ultracentrifugation-based EV depletion.
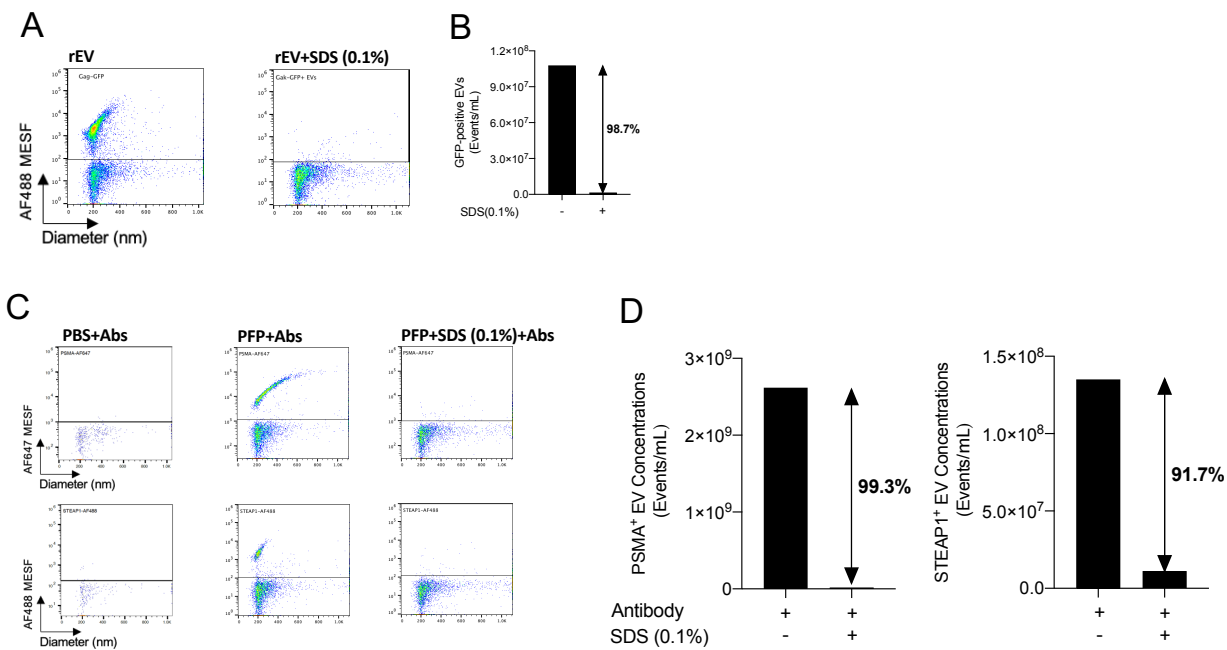
Figure S9. Evaluation of antibody specificity for detection of prostate-derived EVs using detergent-based EV removal in human plasma. (A) Representative cytograms of conditioned medium having recombinant GFP⁺ EVs before and after SDS treatment. (B) Concentrations of recombinant GFP⁺ EVs before and after SDS treatment. (C) Representative cytograms of buffer with antibodies, PSMA-AF647 and STEAP1-AF488 staining of platelet-free plasma sample before and after SDS treatment (D) Comparison of concentrations of PSMA⁺ EVs and STEAP1⁺ EVs before and after SDS treatment of platelet-free plasma.